Controllable superconducting to semiconducting phase transition in topological superconductor 2M-WS_2

Sabin Gautam[1,6], Joseph McBride[2,6], William R. Scougale[1,6], Piumi I. Samarawickrama[1], Danilo De Camargo Branco[3], Peilin Yang[3], ZhuangEn Fu[1], Wenyong Wang[1], Jinke Tang[1], Gary J. Cheng[3], John Ackerman[4], TeYu Chien[1,*], Brian M. Leonard[2,*] and Jifa Tian[1,5*]

[1]Department of Physics and Astronomy, University of Wyoming, Laramie, WY 82071, USA

[2]Department of Chemistry, University of Wyoming, Laramie, WY 82071, USA

[3]School of Industrial Engineering, Purdue University, West Lafayette, IN 47907, USA

[4]Department of Chemical and Biological Engineering, University of Wyoming, Laramie, WY 82071, USA

[5]Center for Quantum Information Science and Technology, University of Wyoming, Laramie, WY 82071, USA

[6]These authors contributed equally: S. Gautam, J. McBride, W. R. Scougale.

*E-mail: tchien@uwyo.edu; bleonar5@uwyo.edu; jtian@uwyo.edu

Abstract

The investigation of exotic properties in two-dimensional (2D) topological superconductors has garnered increasing attention in condensed matter physics, particularly for applications in topological qubits. Despite this interest, a reliable way of fabricating topological Josephson junctions (JJs) utilizing topological superconductors has yet to be demonstrated. Controllable structural phase transition presents a unique approach to achieving topological JJs in atomically thin 2D topological superconductors. In this work, we report the pioneering demonstration of a structural phase transition from the superconducting to the semiconducting phase in the 2D topological superconductor 2M-WS_2. We reveal that the metastable 2M phase of WS_2 remains stable in ambient conditions but transitions to the 2H phase when subjected to temperatures above 150°C. We further locally induced the 2H phase within 2M-WS_2 nanolayers using laser irradiation. Notably, the 2H phase region exhibits a hexagonal shape, and scanning tunneling microscopy (STM) uncovers an atomically sharp crystal structural transition between the 2H and 2M phase regions. Moreover, the 2M to 2H phase transition can be induced at the nanometer scale by a 200 kV electron beam. The electrical transport measurements further confirmed the superconductivity of the pristine 2M-WS_2 and the semiconducting behavior of the laser-irradiated 2M-WS_2. Our results establish a novel approach for controllable topological phase change in 2D topological superconductors, significantly impacting the development of atomically scaled planar topological JJs.

Keywords: 2D materials, 2M-WS_2, phase transition, topological superconductivity, semiconductor

1. Introduction

Topological superconductors, distinguished by their exceptional properties originating from their topological nature, have garnered significant interest due to their potential for hosting Majorana quasiparticles. These exotic quasiparticles are anticipated to offer a resilient foundation for fault-tolerant quantum computation, addressing decoherence problems that commonly affect conventional qubits [1-3]. Approaches for achieving topological superconductors can be divided into three categories [4]: (i) real-space superconducting proximity effect-induced topological superconductivity, exemplified by $Bi_2Te_3/NbSe_2$ [5]; (ii) reciprocal-space superconducting proximity effect-induced topological superconductivity, as observed in doped three-dimensional (3D) topological insulators [6-7] and iron-based superconductors [8-12]; (iii) intrinsic topological superconductivity, as seen in Sr_2RuO_4 [13], UTe_2 [14], and Pb_3Bi [15]. In recent years, substantial progress has been made in exploring realistic material systems that can support robust topological superconductivity [16-17], and researchers have also been working to develop the theoretical foundation for constructing topological qubits as critical components [18-20]. However, topological qubits based on topological Josephson junctions (JJs) derived from topological superconductors have not yet been successfully realized. Future research efforts aimed at addressing the remaining challenges, which encompass material synthesis, device fabrication, and the elucidation of the fundamental relationship between topological superconductivity and Majorana quasiparticles, are of paramount importance.

2D transition metal dichalcogenides (TMDs) have gained significant attention in the field of topological superconductivity, owing to their 2D structure and topological properties [21-26]. For instance, 2M-WS_2 [27-31], a recently discovered 2D topological superconductor, exhibits both captivating topological surface states and robust superconductivity (figure. 1(a)). Notably, bulk

2M-WS_2 demonstrates a critical temperature T_C of ~ 8.8 K [31], the highest among all 2D superconductors in the TMD family. Furthermore, this material exhibits a range of intriguing phenomena, including extremely large magnetoresistance [32], Majorana bound states [27], and topological surface states [28]. On the other hand, 2D TMDs are characterized by polymorphic crystal structures, including 2H, 1T, 1T', and topological 2M phases, which display a wide range of lattice configurations [30-31, 33-35]. The unique symmetries and transition metal coordination environments of these structures dictate the distinct electrical, optical, catalytic, and topological properties of 2D TMDs. In the past decade, notable progress in structural phase transitions between 2H and 1T or 1T' phases in 2D MX_2 atomic layers has been achieved through different techniques, including temperature [36,37], strain [38-40], laser irradiation [41,42], and electrostatic doping [43-45], etc. However, phase transitions between topological superconducting and semiconducting phases (figure 1(a)) or other phases in 2D TMDs are still rare [46,47]. As a result, investigating structural phase transitions in 2D superconductors is crucial for deepening our understanding of their fundamental physical properties and unlocking potential applications in future quantum devices.

In this work, we demonstrate the structural (topological) superconductor-to-semiconductor transition in both WS_2 bulk crystals (figure 1(b)) and atomically thin layers (figure 1(c)). We induced the global and local 2H phase in 2M-WS_2 through three distinctive yet simple techniques including heating, electron beam, and/or laser irradiation. Raman spectroscopy and photoluminescence (PL) measurements were employed to trace the evolution of the structural 2M to 2H phase transition. While no PL signal was detected in the pristine 2M-WS_2 thin layer due to its metallic nature, a distinct PL peak at ~1.9 eV, consistent with intrinsic 2H-WS_2, emerged following the 2M to 2H phase transition. We used selected area electron diffraction (SAED) and

scanning tunneling microscopy (STM) to reveal the corresponding crystal structures of the WS_2 atomic layers. A remarkable discovery is the hexagonal shape of the region with locally induced 2H phase in the 2M-WS_2 layer. The electrical transport measurements provide additional evidence of the non-superconducting nature of laser treated 2M-WS_2 sample. Our findings have the potential to establish a groundbreaking methodology for manipulating the topology and superconductivity properties of 2D topological superconductors. This could significantly enhance the development of functional superconducting quantum devices, with a particular emphasis on the innovative design of topological Josephson junctions in 2D homojunctions.

2. Results and discussion

2.1 Thermal stability of bulk 2M-WS_2

We have successfully grown the high-quality 2M-WS_2 bulk crystal (figure 1(b)) and identified the unconventional superconductivity in its nanolayers [30]. To study the stability of the 2M phase of WS_2, bulk samples of 2M-WS_2 were heated to 400 ºC at different rates (5-25 ºC/min) with Differential Scanning Calorimetry (DSC). Figure 2(a) shows that 2M-WS_2 undergoes an exothermic event starting at 180ºC (heating rate of 5ºC/min). This event appears to be a phase conversion as Thermogravimetric analysis (TGA) shows no significant weight loss correlating to this exothermic event. The kinetics of this phase conversion are studied by following the peak position of the exothermic event signaling the phase change. The exothermic peak positions are observed to increase in temperature corresponding to an increase in heating rate (figure 2(a)). The exothermic peak positions and heating rates are then fitted using equation (1) derived from the Arrhenius equation to extract the activation energy of the phase transition.

$$\ln(k) = \frac{-E_a}{RT} + A \qquad (1)$$

In this equation, k is the heating rate (K/min), E_a is the activation energy of the transition (J/mol), R is the molar gas constant (8.3144 J $mol^{-1}K^{-1}$), T is the temperature at which the exothermic peak is at its maximum, and A is the frequency factor. Figure 2(b) shows the fit of the data to the Arrhenius equation, where the slope of the line is proportional to the activation energy of the phase conversion. The slope of the line in figure 2(b) corresponds to an activation energy of 49.5 kJ/mol for the conversion of the metastable 2M-WS_2 phase to the stable 2H-WS_2 phase.

The crystal structures of the 2M-WS_2 samples before and after heating up to 400ºC using TGA/DSC are characterized by powder X-Ray diffraction (XRD). Figure 2(c) shows the as-made 2M-WS_2 from our simple synthetic method with refined cell parameters of a = 12.85 Å, b = 3.22 Å, c = 5.70 Å, α = γ = 90°, and β = 112.91° which agree well with 2M-WS_2 in literature [30-31]. When sufficient heat is applied, the XRD results show that the crystal structure has changed to the stable hexagonal structure 2H-WS_2 (figure 2(d)). XRD refined cell parameters for the hexagonal converted phase 2H-WS_2 are $a = b$ = 3.172 Å, c = 12.61 Å. This change in lattice parameters indicates a heating-induced structural transition from the 2M phase to the 2H-WS_2 phase, demonstrating the metastability of 2M-WS_2.

2.2 Heating induced 2M to 2H phase transition in WS_2 nanolayers

To study the heating induced 2M to 2H phase transition in the atomically thin 2M-WS_2 layers, we exfoliate few-layer 2M-WS_2 flakes from its bulk crystals and transfer them onto SiO_2/Si (285 nm) substrates (figure S1(a)) inside an argon gas-filled glovebox via the commonly used Scotch tape method [30, 48]. Figure 3(a) (first panel) shows the optical image of the as-prepared 2M-WS_2 thin flake. We then heat the few-layer WS_2 flake on a hot plate in the air at different temperatures from room temperature (RT) to 300 ºC and each for 15 minutes. The corresponding optical images are

shown in figure 3(a), where we see that the contrast of the 2M-WS_2 flake gradually changes from purple to blue as the heating temperature increases. At each temperature, we perform the Raman spectroscopy and PL measurements to identify the evolution of the corresponding 2M to 2H phase transition of the WS_2 flake, as shown in figures 3(b) and (c), respectively. Without heating, the WS_2 thin flake shows the characteristic Raman spectrum (figure 3b and figure S1(b)) of its intrinsic 2M phase, which remains stable in ambient conditions (figure S2) [31]. No change of the Raman spectrum of the 2M-WS_2 thin flake is identified until the temperature reaches 150 ºC, suggesting that the 2M phase can be stable up to this temperature (figure S3). Such an observation is consistent with our theoretical predication a 4L 2M-WS_2 layer based on molecular dynamics simulation (Supplementary Note 1 and figure S4). We note that this result is significant, offering critical insights for the exploration and utilization of the intrinsic properties of 2M WS_2-based quantum devices, which are typically fabricated by standard nanofabrication methods. For instance, for electron beam lithography, a typical baking temperature for polymethyl methacrylate is 180 ºC which is higher than the phase transition temperature of 2M-WS_2. In figure 3(b), compared with the room temperature data, we notice that the intensities of the Raman peaks associated with the 2M phase decrease, and two new active Raman modes appear at ~ 350 cm^{-1} (E_{2g}^1) and 420 cm^{-1} (A_{1g}), indicating the appearance of the 2H phase of WS_2. As we further raise the temperature, the intensities of two new Raman modes substantially increase while those of the 2M phase further decrease. We note that even though 2H phase has been induced, no PL signal can be detected even at the heating temperature of 200 ºC. This is because there may be a significant portion of the 2M phase that can quench the photogenerated electrons. At 250 ºC, the Raman modes of the 2M phase become very weak, while those of the 2H phase are significantly enhanced, suggesting the 2H phase of WS_2 is now dominant (figure S5). Correspondingly, a PL peak near 1.95 eV can be

detected (figure 3(c)). At 300 ºC, the Raman peaks of the 2M phase disappear and the intensities of two characteristics of Raman peaks of 2H-WS_2 at ~ 350 cm^{-1} and ~ 420 cm^{-1} are significantly enhanced, demonstrating a complete 2M to 2H phase transition. Further, we carry out PL (figure 3(c)) measurements to confirm the heating-induced 2H phase of the WS_2 thin flake, where a pronounced PL peak around 1.95 eV has been detected, consistent with that of the pristine few-layer 2H-WS_2 flake (figure S6).

To further reveal the time evolution of the 2M to 2H phase transition, we measure the Raman and PL spectra on another few-layer 2M-WS_2 by heating it on a hot plate at 300 ºC with different time intervals. Figure 3(d) depicts the corresponding optical images of the thin flake on a Si/SiO_2 substrate. We find that the characteristic Raman spectrum (figure 3(e)) of the 2H phase has already been observed after heating for 5 minutes. However, no clear PL peak can be resolved (figure 3(f)). As we extend the heating time, the intensities of the active Raman modes of the 2H phase further increase. In the meantime, the PL signal starts to show up and becomes prominent at ~ 1.92 eV after heating for another period of 30 minutes. We note that the exact positions of the PL peaks may vary among 2H-phase WS_2 flakes with different thicknesses, as shown in figures 3(c), (f) and figures S5 and S6, mainly due to the thickness-dependent band gap of 2H-WS_2 [49].

2.3 Laser irradiation induced local 2M to 2H phase transition in WS_2 thin layers

Inspired by the heating-induced global 2M to 2H phase transition, we further realize the local 2M to 2H phase transition in the 2M-WS_2 atomic layers by laser irradiation. The laser irradiation is performed on few-layer 2M-WS_2 flakes using a 532 nm laser equipped in our Raman system. Figure 4(a) shows the optical image of a 2M-WS_2 thin layer where location 1 (red dot) was irradiated for 30 seconds by the 532 nm laser with a 10% ND filter (~ 4.35 mW). Similar to the

optical images shown in figure 3, we see that the optical contrast at the irradiated region is significantly changed, indicating a possible local 2M to 2H phase transition. To characterize the corresponding structural phases near the laser-irradiated region, we take both the Raman and PL spectra at different locations marked with dots (1-4) in different colors, as shown in figure 4(a). To avoid any possible laser irradiation-induced phase transition while taking the Raman spectra or mapping, we limit the laser power to 0.1% (~ 0.06 mW) at which no phase transition has been detected. Figures 4(b) and (c) show the obtained Raman and PL spectra, respectively. At location 1, the characteristic Raman spectrum of 2H-WS_2 has been detected with a representative PL peak around 1.9 eV. We conclude that the laser irradiation has induced a complete 2M to 2H phase transition at location 1 in the flake, as evidenced by the disappearance of Raman peaks of the 2M phase and the appearance of new Raman active E_{2g}^1 and A_{1g} modes at ~ 350 cm^{-1} and ~ 420 cm^{-1}, respectively. At the edge of the laser irradiated region (location 2), the Raman spectrum (figure 4(b)) is dominated by the 2M phase, while the E_{2g}^1 and A_{1g} modes of 2H phase still can be detected, suggesting a mixed phase of 2M and 2H phases or a possible 1T' phase [50]. Correspondingly, a weak PL peak has been detected as shown in figure 4(c). As we move away from the center of the laser-irradiated region, the two E_{2g}^1 and A_{1g} modes of 2H phase become much weaker at location 3 and are not detectable at location 4 where the crystal structure is 2M phase. Further, at locations 3 & 4, no PL signal has been detected, as shown in figure 4(c). We further demonstrate precise laser patterning the 2M-WS_2 layers to display the letters "U" and "W" (figures 4(d) and (e)) where the 2H phase is locally induced. For this, we employed a 532 nm laser with an approximate power of 4.35 mW, using a step size of 2 μm and an exposure time of 0.1 seconds per point. The spatial confinement of this phase transition was substantiated by mapping the intensities of the characteristic Raman E_{2g}^1 (figure 4(f)) and A_{1g} (figure 4(g)) modes of the 2H

phase. Notably, the pure 2H phase of WS_2 was restricted to the laser-irradiated regions with an approximate diameter of 1 μm, a limitation set by the resolution of the focused laser.

2.4 Scanning tunneling microscopy investigation

Although all the optical measurements indicate the laser-irradiated area has a crystal phase change from 2M to 2H, it is still unclear how the two phases evolve spatially at sub-micron scales. Scanning tunneling microscopy (STM) measurements were conducted to explore this behavior at the atomic scale. Figure 5(a) shows a large-scale STM image of a 2M-WS_2 flake as transferred onto a thin graphite layer, as described in the methods section. This STM image presents a clearly visible laser-irradiated area and allows for a detailed analysis of the structural and electronic properties of the flake at different locations. Surprisingly, we find that the laser-irradiated region shows a hexagonal pattern with a lower height inside in the topography images (figure 5(a)), consistent with the AFM image (figure S7). The depth inside the hexagonal region is determined to be ~7 nm, as seen in the line profile in figure 5(b). Note that the thickness of the non-irradiated area is ~20 nm (figure 5(b)). The height change of the laser-irradiated region could originate from two sources: (1) differences in the vertical stacking height of the 2H and 2M phases and (2) removal of material due to laser exposure. For the different stacking heights to explain the reduction of sample thickness in the laser-irradiated region, the inter-layer spacing for the 2H phase would have to be smaller than that of the 2M phase. However, due to the lattice distortion, the vertical distance between the layers of 2M phase is ~ 5.9 Å, which is thinner than that of the 2H (~ 7.1 Å). Therefore, given the same number of layers of WS_2, the height of its 2H phase should increase compared to the 2M phase. Thus, scenario (1) cannot explain our observation. We believe that the thickness reduction in the laser-irradiated region might be caused by materials removal/evaporation due to local heating or laser ablation. We further notice that the STM tip with

a certain bias can be employed as an effective tool to etch materials from the hexagonal region. In particular, the line profile in figure 5(b) presents a peak at the center, in agreement with earlier STM scans of this structure (figure S8). However, in figure 5(c), we see that the peak structure at the center in figure 5(a) is now replaced with a hole, as well as the topographically lower regions are expanded in the laser irradiated region. To confirm these observations, we have performed AFM measurements on other laser-irradiated regions (figure S7), where the height difference is only around 1-2 nm. We note that the different local density of states between 2H, 1T' and 2M phases may induce different apparent heights in the order of angstrom or smaller, which cannot explain the observed ~10 nm height change. Our results suggest that the increased height difference after STM measurements is mainly due to the etching effect from the STM tip (figure S8). Such a layer-by-layer etching of 2D materials using STM has been demonstrated previously [51]. We further notice that, in all of the samples with laser-irradiated regions, there remains a central region that is equally high as the outer regions away from the laser-irradiated region (figure 5(a) and figure S7). This could have resulted from the laser beam profile or could be a result of the strain relaxation dynamics of the expansion of the *b* axis direction.

Figures 5(c) and (d) show the zoomed-in topographic image and dI/dV mapping of the laser-irradiated region, respectively. From the topography image (figure 5(c)), the boundary of the region with a lower height is highlighted using a dashed hexagon. The size of the hexagonal region is 800 ± 50 nm as illustrated by the line profile (figure 5(b)). Inside this region, we see a clear different dI/dV contrast compared with the exterior regions, indicating a different crystal phase. Interestingly, we find that there is a transition region which extends as far as 50 nm out of the hexagonal boundary. This region shows a different dI/dV contrast compared with interior and

exterior regions (figure 5(d)). This result suggests a third crystal phase may exist in this transition region.

To further determine the crystal structures at different locations of the laser-irradiated 2M-WS_2 thin layer, we have collected the atomically resolved STM images (figures 5(e) to (h)) and the corresponding dI/dV spectra (figure S9). Figures 5(e) and (f) are collected within the interior hexagonal area as identified by the 'e' and 'f' labels in figure 5(c). We see that both regions present clearly hexagonal atomic structures with the same crystal orientation, as further confirmed by the corresponding Fast Fourier Transform (FFT) images. These results demonstrate that the inner region is a single crystal with the 2H phase. Interestingly, scanning in the transition region (~ 50 nm) with differing dI/dV contrast at the upper left corner of the red 'g', outside the hexagonal region contains an atomic resolution of a monoclinic surface structure (figure 5(g)). However, the crystal symmetry is not aligned with the 2M phase observed from the parent crystal far away (figure 5(h)). From the atomically resolved STM image and the corresponding Fast Fourier Transform (FFT) (figure 5(g)), we see that, in this region, the row axis is aligned well with the edge of the hexagonal structure (figure 5(c)). This indicates an interesting phase change, where the crystal phase may be unchanged, but the orientation is, due to thermal effects. Notably, while one set of the additional monoclinic spots is present in figure 5(g) and circled in blue, there is an absent set. These are compared to the FFT collected from the parent crystal, which contains both sets of spots, circled in blue and green respectively in figure 5(h). Although this may be due to the change in the scanning conditions, it also could result from the surface being the similar 1T' phase, which differs only in stacking orientation. Based on the consideration of the measured FFT's, this intermediate region matches better with reported FFT's of 1T' WS_2 [50, 52]. Our results suggest

that while the 2M to 2H phase transition dominates the transition, there are additional physical processes occurring within and along the boundary of the phase-changed region.

2.5 Electron beam irradiation induced 2M to 2H phase transition at the nanometer scale

We further study how the electron beam affects the crystal structural transition in 2M-WS_2. Transmission electron microscopy (TEM) was used to image 2M-WS_2 thin layers as well as collect the corresponding Selected Area Electron Diffraction (SAED) to confirm the crystal structure at the nanometer level. During our analysis, it was noticed that the crystals were slightly reactive to the electron beam (200kV Field Emission Gun). Depending on the spot size and length of exposure, the crystals could be imaged, and diffraction collected to demonstrate the 2M structure as seen in figures 6(a) and (c). Changing the spot size allows more interaction with the electron beam and heating of the sample which converted the same flake into the 2H phase as seen in figures 6(b) and (d). While the crystal appears mostly unchanged other than a slight difference in contrast, the SAED pattern shows a significant change in symmetry associated with the phase change from 2M to 2H. The change, in contrast, is likely due to strain caused by the structural rearrangement and/or symmetry changes at the atomic level interacting with the electron beam differently. Further study of several thin layers showed significant contrast change when the electron beam was spread or defocused, as seen in figures S10(a) to (d). The beam was then brought to crossover or narrowed, and a distinct spot was formed in the WS_2 layer as seen in figure S10. The imaging area was then moved to a different portion of the same crystal but over 100 nm away and repeated to demonstrate the change in contrast with broad beam exposure (figure S10(f) and (g)) and a narrow beam (figure S10(h)). Lattice fringe analysis can also be used to confirm crystal structure (figure S10) but the similarity in lattice spacing makes this more complicated than SAED analysis. The entire crystal can be seen in figure S10(i) with the two different exposed regions of the same crystal at the top

and bottom, demonstrating that the beam interaction and phase change can be controlled at the nm level. Further investigations will explore the amount of energy needed to change the phase and the feature size that can be written or patterned using different accelerating voltages and exposure time.

2.6 Electrical Transport Measurements

We further explored phase transition from superconducting to semiconducting in a partially laser-irradiated 2M-WS_2 thin layers by electrical transport measurements. We have fabricated a high quality nanodevice on the pre-fabricated Hall-bar gold electrodes [30]. Figure 7(a) shows a schematic representation of our laser irradiation procedure on the Hall bar device. To induce the local 2M to 2H phase transition, we irradiate the central region (highlighted with a white dashed rectangle, see figure 7(b) of the device using a 532 nm laser at an approximate power of 4.35 mW. We measured the resistances between different combinations of the electrodes, as shown in figures 7(d) and (e). Resistance measurements between different electrode combinations are depicted in figures 7(d) and (e). Notably, when employing electrodes 6 and 2 as voltage probes, we identified a resistance drop to zero at a transition temperature of 5.7K. Conversely, although a resistance drop was observed, no zero-resistance has been achieved between electrodes 5 and 3, which can be attributed to a partial 2M to 2H phase transition in this region (refer to figure 7(c)). Upon measuring resistances across the laser-irradiated region using either electrodes 6-5 or 2-3 pairs, we observed: 1) the resistance increases to about 21 kΩ, which is three orders of magnitude higher than the pristine 2M-WS_2 sample, and 2) the corresponding temperature dependence shows non superconducting behavior, as shown in figure 7(e). Our transport results further demonstrate the phase transition from superconducting to semiconducting within the laser-irradiated 2M WS_2 thin layer.

3. Conclusion

In summary, we report a novel structural superconductor-to-semiconductor phase transition in both bulk and atomically thin WS_2. Our results demonstrate that the 2M phase of WS_2 is a metastable state, as evidenced by DSC analysis. Notably, the phase transition from 2M to 2H in WS_2 nanolayers can be activated either by heating above 150°C or through electron beam irradiation using a 200 kV Field Emission Gun. Moreover, we have achieved a localized phase transition in atomically thin WS_2 layers from superconducting (2M phase) to semiconducting (2H phase) via laser irradiation, resulting in a distinct hexagonal pattern in the treated regions. STM investigations reveal a nanoscale transition between the 2H and 2M phases, marked by a transitional area of roughly 50 nm. Electrical transport measurements further underscore the non-superconducting nature of the laser-treated 2M-WS_2 sample. In summary, our findings pave the way for innovative applications in the realm of superconducting quantum devices, hinting at the potential for topological superconducting JJs in 2D homojunctions.

4. Methods

4.1 2M-WS_2 crystal synthesis

Sulfur powder was received from Sigma Aldrich, Tungsten metal powder was received from Beantown Chemical, and potassium metal chunks were received from STREM. All reagents were used as received. $K_{0.7}WS_2$ was synthesized from a 0.7:1:2 ratio of potassium metal, tungsten, and sulfur powders in an evacuated Pyrex tube (1 cm x 25 cm). The Pyrex tube was evacuated (2 Pa) and sealed before it was heated at 100°C for one day, then it was cooled and shaken up to mix the reaction mixture. The tube was then heated at 200°C, 300°C, and 400°C for 24 hours each and then ground with a mortar and pestle in an argon atmosphere and a pellet (1cm x 0.25dm) formed.

The pellet was then transferred to a fused quartz tube and heated at 800°C for 48 hours and slowly cooled to 550°C at a rate of 0.1°C/min. The $K_{0.7}WS_2$ crystals were then chemically oxidized to deintercalate the potassium in an aqueous solution of 0.01M $K_2Cr_2O_7$ and 0.02M H_2SO_4 for 1.5 hours and washed with deionized water and then dried in a vacuum oven for 24 hours. Phase purity of $K_{0.7}WS_2$ and the produced 2M-WS_2 was confirmed by XRD with a Rigaku Smart Lab X-ray diffractometer.

4.2 Preparation of 2M-WS_2 atomically thin layers

Silicon substrates (SiO_2/Si with oxide thickness 285 nm) were cleaved into squares (approx. 1cm^2). After cleaving, the substrates were cleaned sequentially by acetone, isopropanol, and deionized water and then dried by nitrogen gas. The 2M-WS_2 thin layers were exfoliated from the bulk crystals using the "Scotch tape" method and then isolated on the SiO_2/Si substrates inside an argon-filled glovebox or in air. We note that there is no noticeable degradation of the samples after exposure to the air.

4.3 Raman and PL measurements

The crystal structure of bulk or exfoliated WS_2 thin flakes was characterized by Raman spectroscopy at room temperature under ambient conditions. Raman measurements were carried out using a 532 nm laser beam with a 100 × objective via a Horiba Raman (XploRA PLUS) system. The laser spot size was ~1 μm and the spectra were collected using 2400 groove/mm diffraction grating. The laser power was regulated using in-build neutral density (ND) filters. To avoid any further local heating on the flake, we only used 0.1% laser power to acquire all the Raman spectrum, where no laser irradiation-induced phase transition has been detected. The powers of the

laser with 0.1% and 10% ND filters are ~ 0.06 mW and 4.35 mW, respectively. The Silicon Raman mode at 520.62 cm^{-1} was used for the calibration prior to the measurement.

PL spectra were recorded at room temperature using a 532 nm laser beam with a 100× objective via the same Horiba Raman (XploRA PLUS) system. The laser spot was ~ 1 μm and the spectra were collected using 600 groove/mm grating.

4.4 Scanning tunneling microscopy measurements

STM measurements were performed to visualize the phase changed region. A thin graphite flake was deposited onto a $Si/SiO_2/Au$ film substrate, with concentric ring structures for flake searching as described in a previous work [30]. Then, a 2M-WS_2 flake was exfoliated and transferred onto the graphite layer to preserve a flat region for STM scanning. The 2M-WS_2 was then exposed to laser illumination with a 10 % power filter for a duration of 1 sec as in the other laser exposure study. STM measurements were then carried out to investigate the laser irradiated region in a Scientia Omicron low temperature scanning tunneling microscope (LTSTM). The base pressure in the STM vacuum system was 3×10^{-11} mbar. The scanning tip was electro-chemically etched tungsten wire and confirmed to be high quality on the nearby graphite area. dI/dV mapping signals were collected using the lock-in technique, with a modulation frequency of 973.1 Hz and an amplitude of 30 mV. Data was processed using WSxM software, and atomic resolution images presented have been Gaussian smoothed using a size 3 kernel within WSxM software to clarify the atomic signal [53].

4.5 TEM and TGA/DSC measurements

TEM images and SAED patterns were collected, on samples sonicated in isopropyl alcohol and drop-cast on copper grids, with a FEI Tecnai G2 F20 200 kV transmission electron microscope. TGA/DSC data was collected using a TA instruments Q600 SDT.

4.6 Device fabrication and electrical transport measurements

The 2M-WS_2 thin layers were mechanically exfoliated from the bulk crystal and transferred onto the SiO_2/Si substrates. The predefined Hall-bar gold electrodes were made on bare SiO_2/Si substrates using the standard nanofabrication techniques. The flake was picked up using a polyvinyl alcohol (PVA) coated Polydimethylsiloxane (PDMS) stamp and transferred to the Hall-bar electrodes using the dry transfer method. The middle region of the device was irradiated using a 532 nm laser with a ~ 4.35mW laser power. The transport properties of the laser irradiated WS_2 thin layers were systematically investigated in an Oxford TeslatronPT system with a base temperature of T = 1.5 K.

Data availability statement

The data that supports the findings of this study are available upon reasonable request from the authors.

Acknowledgments

This research was supported by the U.S. Department of Energy, Office of Basic Energy Sciences, Division of Materials Sciences and Engineering uder awards no. DE-SC0021281 and DE-SC0024188 for material synthsis. And U.S. National Science Foundation (NSF) grant OMA MPS-2228841 for device fabricataion and measurements.

Conflict of interest

The authors declare no competing financial interests.

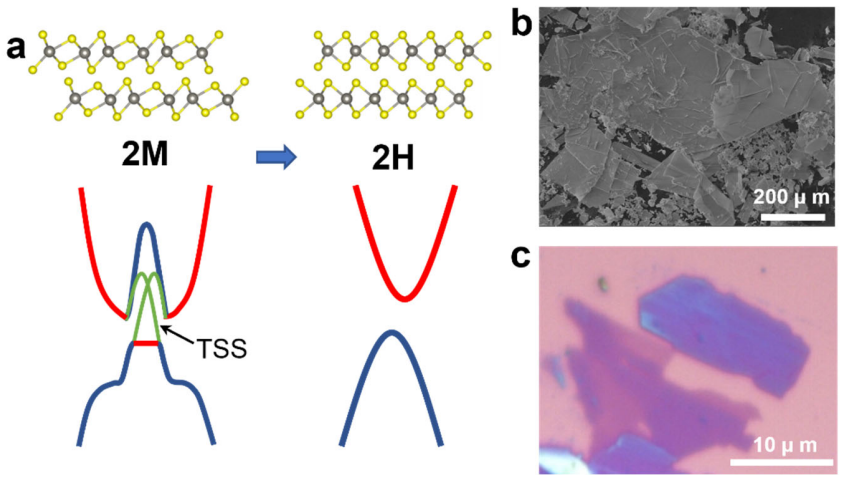

Figure 1. Two types of crystal structures of WS_2 and 2M-WS_2 bulk and thin layer samples. (a) Two structural phases and schematic plots of the corresponding band structures of few-layer 2M- and 2H-WS_2, respectively. The grey atoms are W atoms, and the yellow atoms are S atoms. The green line shows the possible shape of the topological surface states (TSS) of 2M-WS_2. (b) SEM image of the as-grown bulk 2M-WS_2 crystals. (c) Optical image of 2M-WS_2 few layers on a SiO_2/Si substrate.

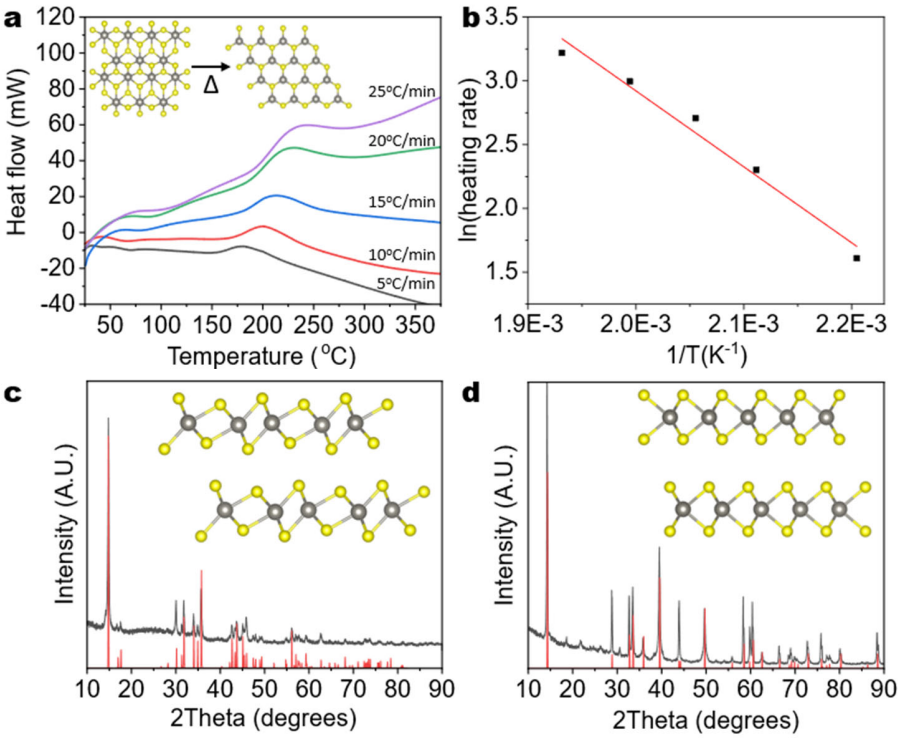

Figure 2. DSC and XRD characterization of bulk 2M-WS_2. (a) DSC for the 2M-2H phase transition as a function of ramp temperature. (b) Kinetic Arrhenius plot for the conversion of 2M- to 2H-WS_2. (c) XRD of 2M-WS_2 before heating, with inset structure of 2M-WS_2 and simulated pattern of 2M. (d) XRD of 2H-WS_2 after heating, with inset structure of 2H-WS_2 and simulated pattern of 2H.

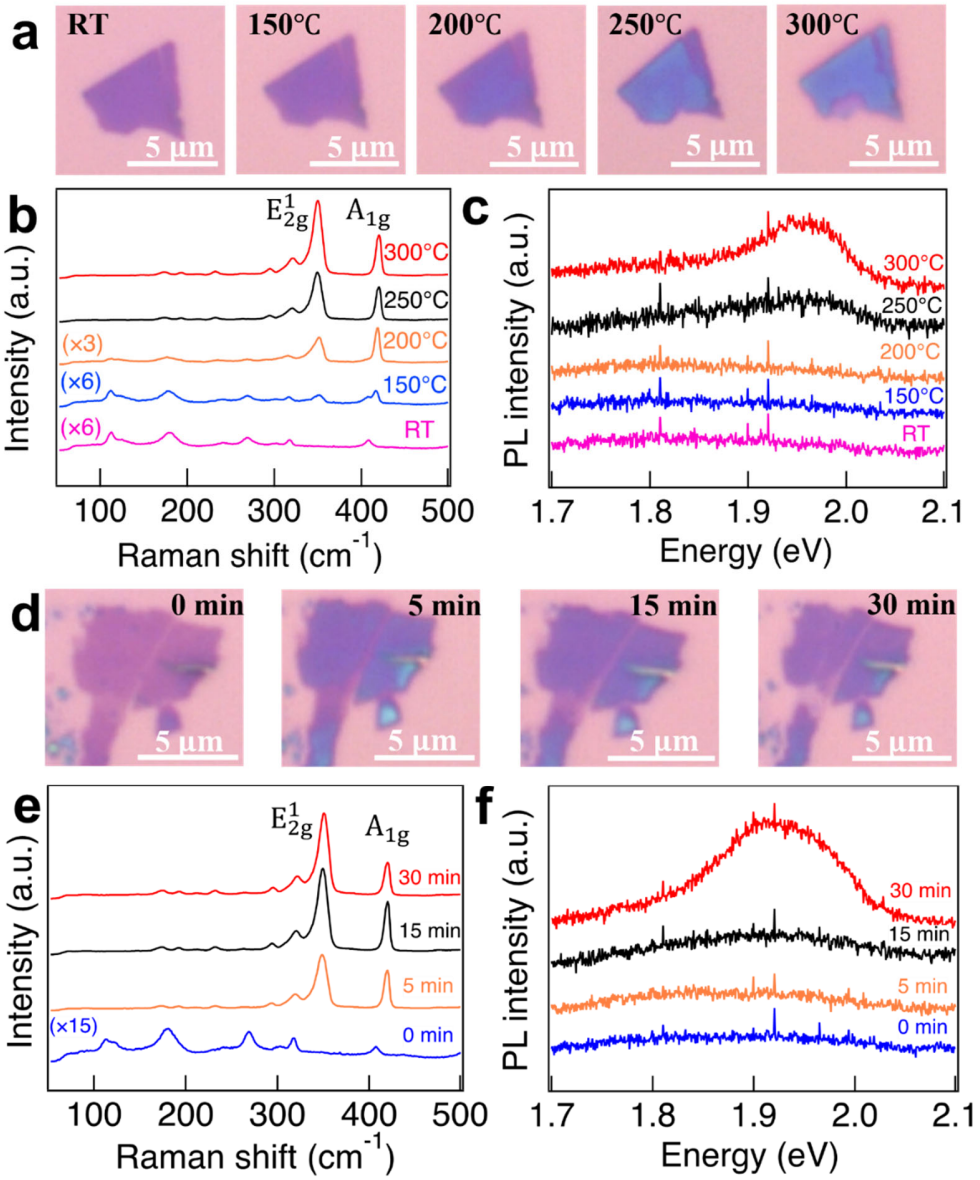

Figure 3. Global 2M to 2H phase transition in WS_2 thin layers induced by heating. (a) Optical images of a few-layer 2M-WS_2 taken after heating for 15 minutes at different temperatures. Corresponding (b) Raman and (c) PL spectrum. (d) Optical images of a few-layer 2M-WS_2 taking after heating for different time intervals at 300 ºC. The scale bar is 5 µm. The corresponding (e)Raman and (f) PL spectrum. RT: Room temperature.

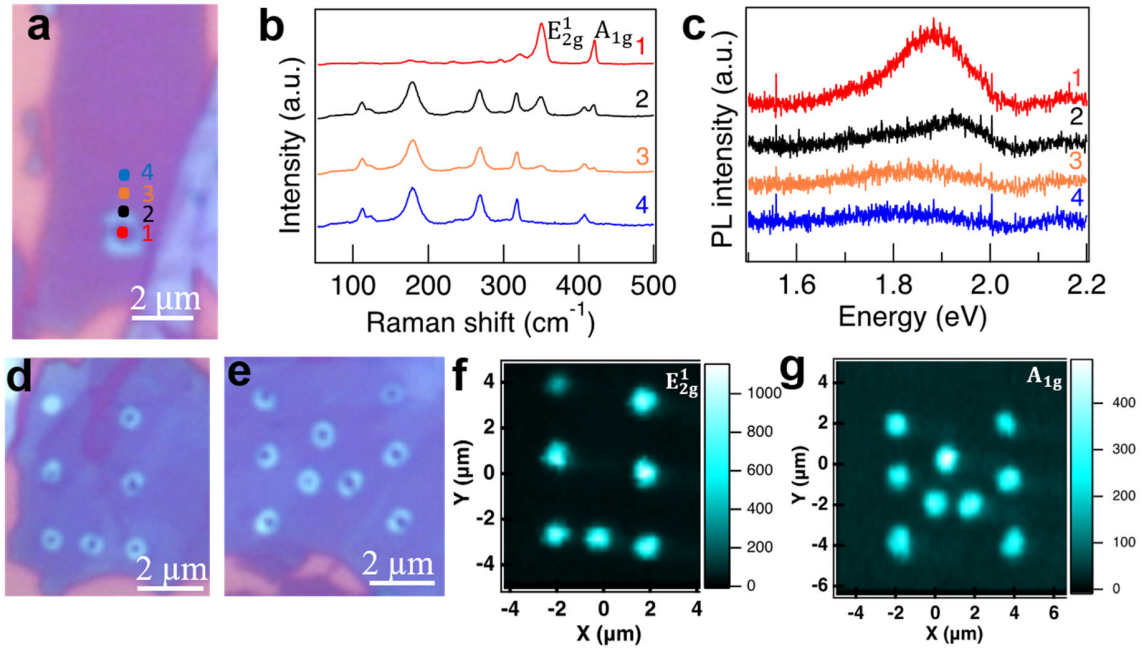

Figure 4. 2M to 2H phase transition in a WS_2 thin layer induced by laser irradiation. (a) Optical image of a few-layer 2M-WS_2. Position 1 on the flake was irradiated by a 532 nm laser with 10% of the power for 30 s. Corresponding (b) Raman and (c) PL spectrum taken at positions 1, 2, 3, and 4 of the flake. Optical images of 2M-WS_2 layers patterned with the letters "U" (d) and "W" (e) using a 532 nm laser at 10% power with an exposure time of 0.1 s per point. Corresponding Raman maps of the E^1_{2g} (f) and A_{1g} (g) modes for d and e, respectively. All the Raman spectra were taken using 0.1% of the laser power.

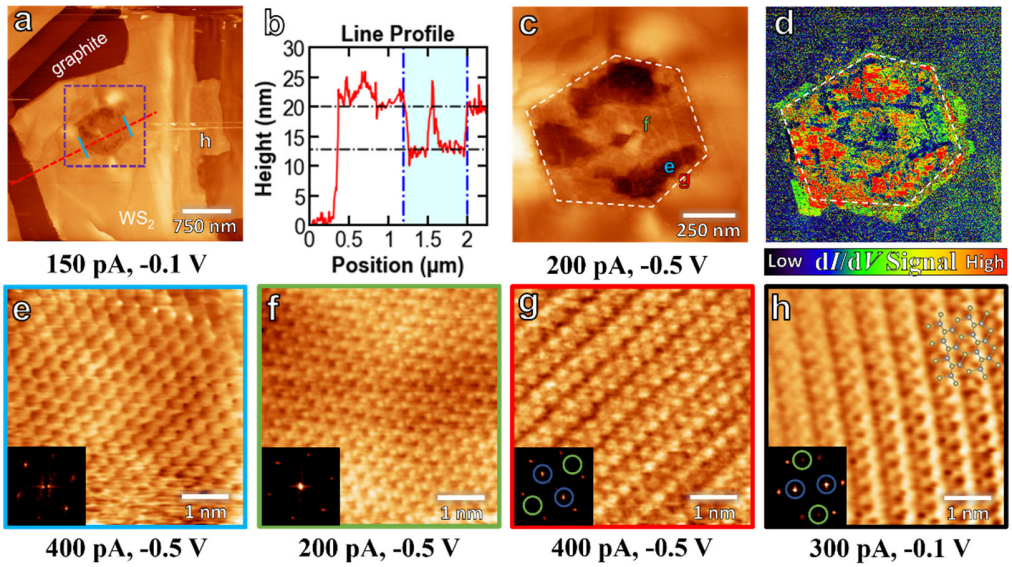

Figure 5. Meso-scale structure of the 2H region, and atomic scale phase visualization. (a) STM topography image of a 2M-WS_2 flake near the laser irradiated region. (b) Line profile taken from a indicating the flake thickness and depth. (c) STM topography mapping showing the laser irradiated region topography. (d) STM dI/dV mapping showing sharp meso-scale hexagonal phase boundary symmetry. (e)-(h) Atomic resolution images of the four regions identified in (a) and (c). Insets are 2D Fast Fourier Transform from respective images.

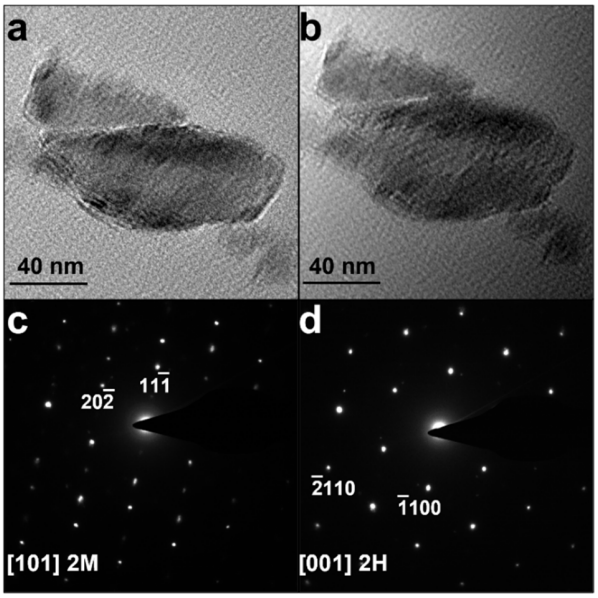

Figure 6. Electron beam induced structural phase transition. Transmission Electron Microscopy (TEM) images and Selected area diffraction (SAED) of a 2M-WS_2 flake (a), (c) as synthesized and (b), (d) after extended exposure to the electron beam showing the change in crystal structure, respectively.

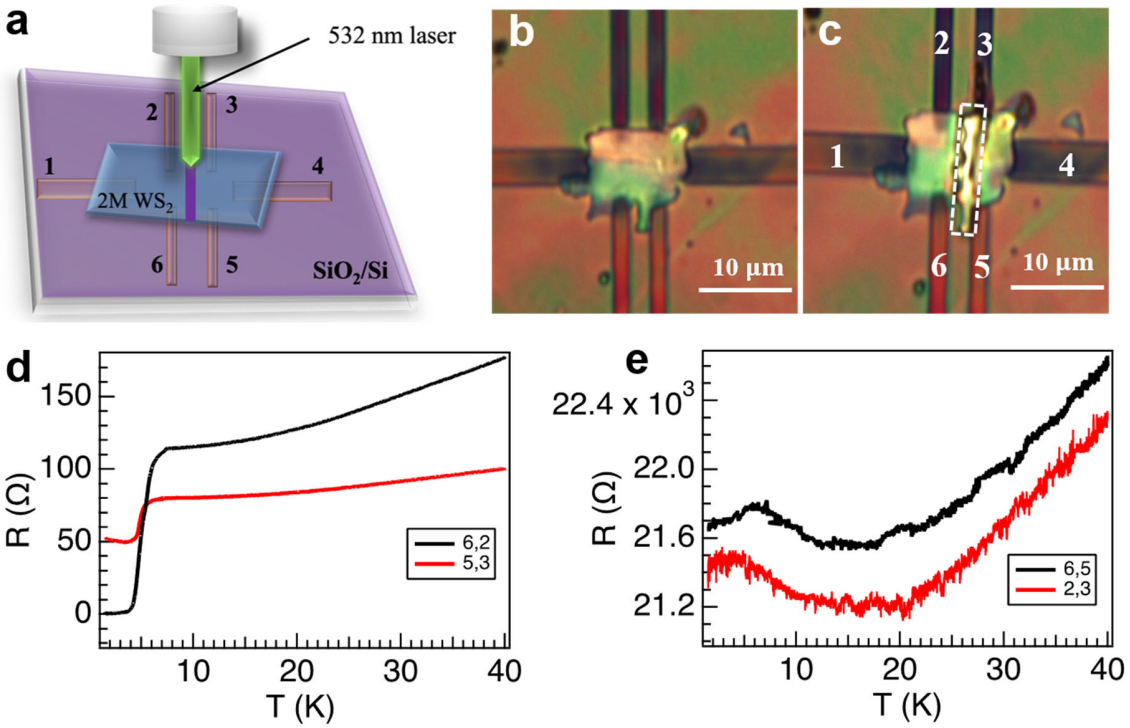

Figure 7. Electrical transport measurements on a partially laser irradiated few-layer 2M-WS_2. (a) The schematic of laser irradiation on the Hall bar device. The optical image of the device before (b) and after (c) laser irradiation. The few-layer 2M-WS_2 flake is covered with a PVA layer, and the laser irradiated region is highlighted with a white dashed rectangle. (d) The temperature dependences of resistance measured between the 5,3 (red) and 6,2 (black) electrodes. (e) The temperature dependences of resistance between the 6,5 and 2,3 electrodes, showing no superconductivity. The bias voltage is applied between 1 and 4 electrodes.

Reference

[1] Qi X L, Zhang S C 2011 Topological insulators and superconductors *Rev. Mod. Phys.* **83** 1057-1110

[2] Alicea J 2012 New directions in the pursuit of Majorana fermions in solid state systems *Rep. Prog. Phys.* **75** 076501

[3] Sharma M M, Sharma P, Karn N K, Awana V P S 2022 Comprehensive review on topological superconducting materials and interfaces *Supercond. Sci. and Technol.* **35** 083003

[4] Qin W, Gao J, Cui P, Zhang Z 2023 Two-dimensional superconductors with intrinsic p-wave pairing or nontrivial band topology *Sci. China Phys. Mech. Astron.* **66** 267005

[5] Xu J P *et al* 2014 Artificial Topological Superconductor by the Proximity Effect *Phys. Rev. Lett.* **112** 217001

[6] Hor Y S *et al* 2010 Superconductivity in $Cu_xBi_2Se_3$ and its Implications for Pairing in the Undoped Topological Insulator *Phys. Rev. Lett.* **104** 057001

[7] Levy N *et al* 2013Experimental Evidence for s-Wave Pairing Symmetry in Superconducting $Cu_xBi_2Se_3$ Single Crystals Using a Scanning Tunneling Microscope *Phys. Rev. Lett.* **110** 117001

[8] Xu G, Lian B,Tang P, Qi X L, Zhang S C 2016 Topological Superconductivity on the Surface of Fe-Based Superconductors *Phys. Rev. Lett.* **117** 047001

[9] Shi X *et al* 2017 $FeTe_{1-x}Se_x$ monolayer films: towards the realization of high-temperature connate topological superconductivity *Sci. Bull.* **62** 503-507

[10] Li M *et al* 2022 Ordered and tunable Majorana-zero-mode lattice in naturally strained LiFeAs *Nature* **606** 890-895

[11] Wang Z *et al* 2020 Evidence for dispersing 1D Majorana channels in an iron-based superconductor *Science* **367** 104-108

[12] Kong L *et al* 2019 Half-integer level shift of vortex bound states in an iron-based superconductor *Nat. Phys.* **15** 1181-1187

[13] Maeno Y *et al* 1994 Superconductivity in a layered perovskite without copper *Nature* **372** 532-534

[14] Jiao L *et al* 2020 Chiral superconductivity in heavy-fermion metal UTe_2 *Nature* **579** 523-527

[15] Qin S, Kim J, Niu Q, Shih C K 2009 Superconductivity at the Two-Dimensional Limit *Science* **324** 1314-1317

[16] Beenakker C W J 2013 Search for Majorana Fermions in Superconductors *Annu. Rev. Condens. Matter Phys.* **4** 113-136

[17] Val'kov V V *et al* 2022 Topological superconductivity and Majorana states in low-dimensional systems *Phys. Usp.* **65** 2

[18] Flensberg K, von Oppen F, Stern A 2021 Engineered platforms for topological superconductivity and Majorana zero modes *Nat. Rev. Mater.* **6** 944-958

[19] Nayak C, Simon S H, Stern A, Freedman M, Das Sarma S. 2008 Non-Abelian anyons and topological quantum computation *Rev. Mod. Phys.* **80** 1083-1159

[20] Read N 2012 Topological phases and quasiparticle braiding *Phys. Today* **65** 38-43

[21] Ajayan P, Kim P, Banerjee K 2016 Two-dimensional van der Waals materials *Phys. Today* **69** 39-44

[22] Buscema M *et al* 2015 Photocurrent generation with two-dimensional van der Waals semiconductors *Chem. Soc. Rev.* **44** 3691-3718

[23] Chaves A, Azadani J G, Özçelik V O, Grassi R, Low T 2018 Electrical control of excitons in van der Waals heterostructures with type-II band alignment *Phys. Rev. B* **98** 121302

[24] Choi Y B *et al* 2020 Evidence of higher-order topology in multilayer WTe_2 from Josephson coupling through anisotropic hinge states *Nat. Mater.* **19** 974-979

[25] Gong C, Zhang X 2019 Two-dimensional magnetic crystals and emergent heterostructure devices *Science* **363** eaav4450

[26] Hidding J, Guimarães M H D 2020 Spin-Orbit Torques in Transition Metal Dichalcogenide/Ferromagnet Heterostructures *Front. Mater.* **7** 594771

[27] Yuan Y *et al* 2019 Evidence of anisotropic Majorana bound states in 2M-WS_2 *Nat. Phys.* **15** 1046-1051

[28] Li Y W *et al* 2021 Observation of topological superconductivity in a stoichiometric transition metal dichalcogenide 2M-WS_2 *Nat. Commun.* **12** 2874

[29] Cho S *et al* 2022 Direct Observation of the Topological Surface State in the Topological Superconductor 2M-WS_2 *Nano Lett.* **22** 8827-8834

[30] Samarawickrama P *et al* 2021 Two-Dimensional 2M-WS_2 Nanolayers for Superconductivity *ACS Omega* **6** 2966-2972

[31] Fang Y *et al* 2019 Discovery of Superconductivity in 2M WS_2 with Possible Topological Surface States *Adv. Mater.* **31** 1901942

[32] Fang Y Q, Wang D, Zhao W, Huang F Q 2020 Large magnetoresistance in the monoclinic 2M WSe_2 *Europhys. Lett.* **131** 10005

[33] Kappera R *et al* 2014 Phase-engineered low-resistance contacts for ultrathin MoS_2 transistors *Nat. Mater.* **13** 1128-1134

[34] Wilson J A, Yoffe A D 1969The transition metal dichalcogenides discussion and interpretation of the observed optical, electrical and structural properties *Adv. Phys.* **18** 193-335

[35] Fang Y *et al* 2019 Observation of superconductivity in pressurized 2M WSe_2 crystals *J. Mater. Chem. C* **7** 8551-8555

[36] Keum D H *et al* 2015 Bandgap opening in few-layered monoclinic $MoTe_2$ *Nat. Phys.* **11** 482-486

[37] Cheon Y, Lim S Y, Kim K, Cheong H 2021 Structural Phase Transition and Interlayer Coupling in Few-Layer 1T′ and Td $MoTe_2$ *ACS Nano* **15** 2962-2970

[38] Hou W *et al* 2019 Strain-based room-temperature non-volatile $MoTe_2$ ferroelectric phase change transistor *Nature Nanotechnol.* **14** 668-673

[39] Zhao C *et al* 2020 Strain Tunable Semimetal--Topological-Insulator Transition in Monolayer 1T' WTe_2 *Phys. Rev. Lett.* **125** 046801

[40] Duerloo K A N, Li Y, Reed E J 2014 Structural phase transitions in two-dimensional Mo- and W-dichalcogenide monolayers *Nat. Commun.* **5** 4214

[41] Cho S *et al* 2015 Phase patterning for ohmic homojunction contact in $MoTe_2$ *Science* **349** 625-628

[42] Tan Y *et al* 2018 Controllable 2H-to-1T′ phase transition in few-layer $MoTe_2$ *Nanoscale* **10** 19964-19971

[43] Li Y, Duerloo K A N, Wauson K, Reed E J 2016 Structural semiconductor-to-semimetal phase transition in two-dimensional materials induced by electrostatic gating *Nat. Commun.* **7** 10671

[44] Zhang F *et al* 2019 Electric-field induced structural transition in vertical $MoTe_2$ and $Mo_{1-x}W_xTe_2$-based resistive memories *Nat. Mater.* **18** 55-61

[45] Wang Y *et al* 2017 Structural phase transition in monolayer $MoTe_2$ driven by electrostatic doping *Nature* **550** 487-49

[46] Guan Y *et al* 2023 Femtosecond Laser-Driven Phase Engineering of WS_2 for Nano-Periodic Phase Patterning and Sub-ppm Ammonia Gas Sensing *Small* 2303654 DOI: 10.1002/smll.202303654

[47] Song X *et al* 2023 Acid-Assisted Soft Chemical Route for Preparing High-Quality Superconducting 2M-WS_2 *Chem. Mater*. **35** 5487-5496

[48] Novoselov K S *et al* 2004 Electric field effect in atomically thin carbon films *Science* **306** 666-669

[49] Zhao W *et al* 2013 Evolution of Electronic Structure in Atomically Thin Sheets of WS_2 and WSe_2 *ACS Nano* **7** 791-797

[50] Pierucci D *et al* 2019 Evidence for a narrow band gap phase in 1T′ WS_2 nanosheet *Appl. Phys. Lett.* **115** 032102

[51] Harmer M A, Fincher C R, Parkinson B A 1991 Scanning tunneling microscopy of the surface topography and surface etching of nanoscale structures on the high-temperature superconductors *J. Appl. Phys.* **70** 2760-2763

[52] Mahler B, Hoepfner V, Liao K, Ozin G A 2014 Colloidal Synthesis of 1T-WS_2 and 2H-WS2 Nanosheets: Applications for Photocatalytic Hydrogen Evolution *J. Am. Chem. Soc.* **136** 14121-14127

[53] Horcas I, Fernández R, Gómez-Rodríguez J M, Colchero J, Gómez-Herrero J, Baro A M 2007 WSXM: A software for scanning probe microscopy and a tool for nanotechnology *Rev. Sci. Instrum.* **78** 013705F